Retrieval of atmospheric ozone profiles from an infrared quantum cascade laser heterodyne radiometer: results and analysis

Damien Weidmann,* William J. Reburn, and Kevin M. Smith

Space Science and Technology Department, STFC Rutherford Appleton Laboratory, Didcot, Oxfordshire, OX11 0QX, UK

*Corresponding author: d.weidmann@rl.ac.uk

Received 14 June 2007; revised 21 August 2007; accepted 22 August 2007;
posted 22 August 2007 (Doc. ID 84152); published 4 October 2007

Following the recent development of a ground-based prototype quantum cascade laser heterodyne radiometer operating in the midinfrared, atmospheric ozone profile retrievals from a solar occultation measurement campaign performed at the Rutherford Appleton Laboratory on 21 September 2006 are presented. Retrieval is based on the optimal estimation method. High resolution ($0.0073\ cm^{-1}$) atmospheric spectra recorded by the laser heterodyne radiometer and covering a microwindow ($1033.8–1034.5\ cm^{-1}$) optimized for atmospheric ozone measurements were used as measurement vectors. As part of the evaluation of this novel instrument, a comprehensive analysis of the retrievals is presented, demonstrating the high potential of quantum cascade laser heterodyne radiometry for atmospheric sounding. Vertical resolutions of 2 km near the ground and about 3 km in the stratosphere were obtained. The information content of the retrieval was found to be up to 48 bits, which is much higher than any other passive ground-based instrument. Frequency mismatches of several absorption peaks between the forward model and experimental spectra have been observed and significantly contribute to the retrieval noise error in the upper-troposphere lower-stratosphere region. Retrieved ozone vertical profiles were compared to ozonesonde data recorded at similar latitudes. The agreement is generally excellent except for the 20 to 25 km peak in ozone concentration, where ozonesonde data were found to be 20% lower than the amount retrieved from the laser heterodyne radiometer spectra. Quantum cascade laser based heterodyne radiometry in the midinfrared has been demonstrated to provide high spectral resolution and unprecedented vertical resolution for a passive sounder in a highly compact and mechanically simple package. © 2007 Optical Society of America

OCIS codes: 010.4950, 120.5630, 040.2840, 040.3060, 120.0280.

1. Introduction

A ground-based quantum cascade laser heterodyne radiometer (LHR) operating in the midinfrared and dedicated to sounding atmospheric ozone has recently been developed and deployed during a solar occultation measurement campaign [1]. The main specifications of the instrument are given in Table 1. A quantum cascade laser (QCL) was used as the local oscillator of the LHR. QCLs fit the specifications required for this component that is critical in any heterodyne system: several milliwatts of optical power, spectral purity in the kHz to MHz range, and single mode operation. They also have the advantage of continuous frequency tuning over a specific spectral window (spanning approximately 1% of the central frequency). This particular feature of QCLs is used here to record atmospheric transmission spectra without radio frequency analysis. In addition, QCLs are extremely compact, robust, and reliable devices, all of which make QCL-based sensing instruments ideal for deployment in the field.

During this study, ozone was chosen as the target species. Ozone is present in both the stratosphere (accounting for 90% of the ozone total column) and in the troposphere (10% of the total column). The naturally occurring stratospheric component plays the important role of protecting the biosphere from UVB radiation. Ozone is highly reactive, plays an impor-

0003-6935/07/297162-10$15.00/0

Table 1. Specifications of the Laser Heterodyne Radiometer

Parameter	Capability	During Measurements
Frequency coverage	1025–1037 cm^{-1}	1032.3–1034.5 cm^{-1}
Resolution	<10 MHz–6 GHz double sideband	220 MHz double sideband
Field of view	Dependent on collection mirror diameter	0.25 mrad (50 mm diameter mirror)
Viewing modes	To be investigated	Solar occultation

tant role in the Earth's radiation balance, and participates in stratospheric photochemistry. Human activities, and the chemical emissions associated with them, have depleted stratospheric ozone and increased concentrations in the troposphere. The well known Antarctic stratospheric "ozone hole" was, and still is, caused by previous emissions of chlorofluorocarbon and hydrochlorofluorocarbon molecules; volatile organic compounds and nitric oxides (NO_x) produced by combustion are responsible for increased tropospheric ozone concentrations. In urban areas, episodes of high ozone concentration are increasingly frequent during hot and sunny days. In the boundary layer, photochemically produced ozone is a polluting oxidant with major implications for human health starting at mixing ratios below 0.2 ppmv [2]. Monitoring of tropospheric ozone with a high latitudinal, longitudinal, and vertical resolution is required for the development of models for improved air quality forecasting with a resolution down to the urban area scale.

Optical heterodyne spectroradiometry has successfully been used to measure stratospheric ozone from the ground using either a CO_2 laser or lead salt lasers as local oscillators [3–6]. As QCLs have become matured infrared sources, we developed a ground-based prototype LHR to evaluate the performance of QCL-based optical heterodyne radiometry for remote sensing, with the long term prospect of satellite deployment. In the meantime, aircraft and high altitude platforms are potential candidates for LHR field deployment. Current high-resolution IR radiometers are based on Fourier transform spectrometers. These instruments require large optical path differences to achieve high spectral resolution, and hence large physical size and mass. Current operational satellite instruments of this kind include the Tropospheric Emission Sounder (TES, 0.015 cm^{-1} resolution in limb sounding mode) and the Michelson Interferometer for Passive Atmospheric Sounding (MIPAS, 0.035 cm^{-1} resolution in limb sounding mode). These types of instrument require high accuracy mechanical motions, which are not desirable on a satellite platform. More generally, current space-borne ozone monitoring instruments struggle with providing tropospheric sensitivity [7–9]. A full and detailed discussion on the accuracy and precision of current ozone profile measurements from satellite instruments can be found in Ref. [10]. By comparison, LHRs could bring the cumulative benefits of high spatial resolution (particularly relevant to anthropogenic emission and urban area monitoring and for increased vertical resolution in limb sounding mode), ultrahigh spectral resolution down to and even below 0.001 cm^{-1}, and high sensitivity (shot-noise limited operation). From space the high spectral resolution of the LHR would allow improved resolution of the stratospheric ozone contribution that normally screens ozone in the troposphere, and the intrinsically small field of view would increase the proportion of useful data obtained from partially cloudy scenes.

As far as ground based instruments are concerned, passive remote sensing of atmospheric ozone is currently undertaken using Fourier transform spectrometers [11,12] or UV spectrometers [13,14]. Lidars [15] are also available, but as active sensing instruments they will not be considered in this work. Most existing ground-based passive instruments do not provide enough vertical resolution and merely measure total column abundances.

Recent work on retrieving atmospheric ozone profiles from a ground-based LHR has been reported by Fast *et al.* [16] with an emphasis on the stratospheric component. Ozone abundance in the Martian atmosphere has also been measured by an LHR [17], benefiting from the high sensitivity and the high resolution achievable by infrared laser heterodyne radiometry. In both of these studies, the remote sensing instrument was a LHR based on a CO_2 laser and utilized filter banks for radio frequency (RF) analysis.

This paper presents an analysis of atmospheric ozone profile measurements retrieved from the data recorded with a QCL-based LHR operating in the swept local oscillator frequency mode. Measurements were made from the Rutherford Appleton Laboratory site (Oxfordshire, UK) on 21 September 2006. A full instrument description and details about the measurements have been reported in Ref. [1]. Vertical profiles of atmospheric ozone were retrieved from the measurements using the optimal estimation method (OEM). The first section of this paper provides a brief description of the OEM retrieval method. The second part presents ozone profiles retrieved from the LHR measurements including error and information content analysis.

2. Retrieval Method

Retrievals were performed using the OEM approach. The problem was further constrained by using climatological ozone *a priori* data. This approach strictly follows the method described by C. Rodgers [18]. The forward model F is described by

$$\mathbf{y} = F(\mathbf{x}) + \boldsymbol{\varepsilon}. \quad (1)$$

The state vector **x** contains the vertical profile of atmospheric ozone (the only information to be retrieved here), which was expressed in the logarithm of volume mixing ratios (vmr). Using the logarithm

Table 2. Summary of the Parameters Used in the Retrieval Algorithm

State Vector $\mathbf{x}$	Measurement Vector $\mathbf{y}$	*A Priori* Covariance Matrix $\mathbf{S_a}$	Measurement Covariance Matrix $\mathbf{S_a}$	Forward Model	ILS
O_3 profile (log of vmr)	Atmospheric transmission recorded by the LHR	Diagonal, equal to 1 except for the stratospheric peak values, equal to 0.09	Diagonal, based on a shot noise limited instrument with a degradation factor of 10	RFM including O_3, H_2O, CO_2, NH_3, N_2O, CH_4, $C_2Cl_2F_3$, and $C_2Cl_2F_4$	Obtained from RF filter characteristics; see Fig. 1
Dimension 12	Dimension 998	Dimension 12 × 12	Dimension 998 × 998		

ensures a positive value of the retrieved vmr and was found to yield a better retrieval. However, using the logarithm can introduce undesirable effects and can make it harder for the algorithm to retrieve very low ozone values in a layer where the *a priori* ozone values are large [19]. As is shown below, we used two different sets of *a priori* data to perform retrievals, and no such effect was observed. The measurement vector $\mathbf{y}$ represents an atmospheric transmission spectrum obtained with the LHR; the dimension of the vector is 998 and is related to the local oscillator frequency scan rate used during the measurements. Among the set of data recorded with the LHR, the measurement vector containing the largest amount of information was chosen to perform the retrieval (information analysis is presented in a latter section). $\boldsymbol{\varepsilon}$ is the error associated with the measurements and has the same dimension as the measurement vector.

Atmospheric transmission was calculated using the Reference Forward Model (RFM) [20], which is a high-resolution line-by-line algorithm originally developed for Michelson interferometer for passive atmospheric sounding (MIPAS) data analysis. Spectroscopic data were taken from the HITRAN 2004 database [21]; the species included in the model were O_3, H_2O, CO_2, NH_3, N_2O, CH_4, $C_2Cl_2F_3$, and $C_2Cl_2F_4$. Water vapor, temperature and pressure profiles were obtained from the European Center for Medium range Weather Forecasts (ECMWF) [22]. Data were interpolated from the latitude and longitude grid of the dataset to match the exact location and time of the measurements. For other atmospheric species, typical midlatitude daytime concentration profiles were used. Table 2 summarizes the different parameters used in the retrieval of ozone profiles.

The OEM algorithm minimizes a cost function χ^2 defined as

$$\chi^2 = (\mathbf{y} - F(\mathbf{x}_n))\mathbf{S}_\varepsilon{}^{-1}(\mathbf{y} - F(\mathbf{x}_n))^T + (\mathbf{x_a} - \mathbf{x}_n)\mathbf{S_a}{}^{-1}(\mathbf{x_a} - \mathbf{x}_n)^T, \tag{2}$$

where $\mathbf{S}_\varepsilon$ is the measurement covariance matrix, $\mathbf{S_a}$ is the *a priori* covariance matrix, and $\mathbf{x_a}$ is the *a priori* ozone profile. Thus, minimizing χ^2 amounts to minimizing the weighted differences between the measurement vector and what is expected given the current state vector (the first term in the sum), and between the current state vector and the *a priori* (the second term). Weighting is introduced by covariance matrices describing the uncertainty in both the *a priori* and the measurement vector.

The problem is moderately nonlinear and is solved using local linearization in the iterative Levenberg–Marquardt approach, where

$$\mathbf{x}_{i+1} = \mathbf{x}_i + \left[(1+\lambda)\mathbf{S_a}{}^{-1} + \mathbf{K}_i{}^T\mathbf{S}_\varepsilon{}^{-1}\mathbf{K}_i\right]^{-1} \times \left[\mathbf{K}_i{}^T\mathbf{S}_\varepsilon{}^{-1}(\mathbf{y}_i - F(\mathbf{x}_i)) + \mathbf{S_a}{}^{-1}(\mathbf{x_a} - \mathbf{x}_i)\right]. \tag{3}$$

The $\mathbf{K}$ matrix is the Jacobian matrix (or weighting functions). λ is the Levenberg–Marquardt parameter. In the linear approximation the forward model can be rewritten from Eq. (1) as

$$\mathbf{y} = \mathbf{Kx} + \boldsymbol{\varepsilon}. \tag{4}$$

The covariance matrices were set to be diagonal. $\mathbf{S}_\varepsilon$ was built based on the ideal signal-to-noise ratio (SNR) of the LHR. An additional degradation factor of 10 was introduced to take into account discrepancies between the real instrument and the ideal model. $\mathbf{S_a}$ was built in a conservative way: The relative error in the volume mixing ratio was set at 100%, except for the stratospheric peak values where the relative error was set at 30% to reflect a more accurate climatology and less variability in the stratosphere. Two different *a priori* datasets were tested: The first one was a typical midlatitude daytime ozone profile constructed for MIPAS operational processing (described in Ref. [20]), the second one was the profile interpolated in space and time from the ECMWF data.

During the measurement campaign the spectral resolution of the instrument was set to 220 MHz ($0.0073\ \mathrm{cm}^{-1}$). A 200 MHz high-pass filter rejected the lower frequencies that were prone to higher RF noise. As reported in Ref. [23], the QCL exhibited a large amount of noise in the 0 to 300 MHz range, and rejection of this band improves the SNR. The instrument lineshape (ILS) was accurately measured so

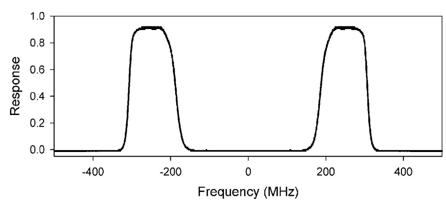

Fig. 1. Plot of the measured LHR instrument lineshape.

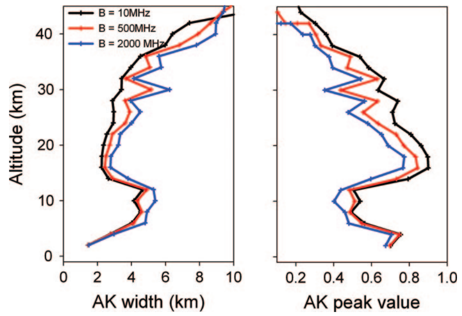

Fig. 2. (Color online) Simulated analysis of the averaging kernels of the ozone profile retrieval from the infrared quantum cascade laser heterodyne radiometer. Calculations for three different double sideband resolutions are presented with the instrument SNR being kept constant.

that it could be included in the forward model, since knowledge of the ILS is essential to extract information from absorption lineshapes. Figure 1 shows the LHR ILS as it has been measured. The purely electronic origin of the ILS and the fact that measuring it is simple and accurate is an additional advantage of the LHR over some other types of passive instrument.

3. Retrieval Simulation

To determine the most appropriate altitude grid, analyses were carried out based purely on RFM simulations and a theoretical model of the instrument. We considered an ideal ground-based instrument working in the solar occultation mode and operating in the 1033.8 to 1034.5 cm^{-1} spectral window, corresponding to a single and continuous QCL frequency scan. This microwindow had been previously identified to minimize the retrieval error for atmospheric ozone [1]. The spectral grid spacing was set to 0.0006 cm^{-1} in accordance with that used during measurements. This sampling interval was physically determined by the temperature tuning rate applied to the quantum cascade laser and the integration time. As a result, the spectral grid is ~6 times smaller than the single sideband resolution, which makes the spectrum slightly oversampled. The solar elevation angle was set to 36°, corresponding to the measurements. A dense grid was used for the analysis of the averaging kernels (AKs): from 0 to 74 km with a 2 km step. The *a priori* covariance matrix used in the simulation was set to be diagonal with a value of 1, corresponding to a relative uncertainty of 100%. The width of AKs provides an estimate of the vertical resolution, and the peak value gives an estimate of the amount of information that can be retrieved from a particular atmospheric layer. These two quantities are closely related, as AKs should be normalized to 1 where the retrieval is accurate.

Figure 2 shows the results of the calculation for three different LHR spectral resolutions (double sideband). The figure was generated by keeping the SNR constant. In this case the advantage of working at high resolution starts to be significant at midtropospheric altitudes and above. It should be noted a higher resolution means a longer integration time, since the SNR remains constant. A dip in AK sensitivity (and a corresponding decrease in vertical resolution) can be observed in the upper troposphere where O_3 concentration is at a minimum. Figure 2 also indicates that no reliable information can be obtained with the ground based LHR for altitudes higher than 40 km. The following altitude grid was chosen for the retrievals: 1, 3, 5, 10, 13, 16, 19, 22, 26, 30, 35, and 40 km.

An interesting outcome from the calculation is the total insensitivity of the AKs to the central dip in the ILS, apparent in Fig. 1. The RF noise floor decreases toward higher frequencies. Consequently, rejecting the lowest RF frequencies brings great advantage since operation approaches the theoretical shot noise limit with no adverse effects on the quality of the atmospheric profile retrieval. In the present work, the low frequency rejection was 0 to 190 MHz. The folding effect that this rejection introduces does make the recorded spectrum ambiguous for the purposes of spectral line assignment. However, as long as the characteristics of the spectral lines are well known and included in the forward model, there is absolutely no other effect, except to improve the quality of the measurements.

During this analysis the effect of the size of the spectral window was investigated. The LHR uses the continuous frequency tuning capability of the QCL to

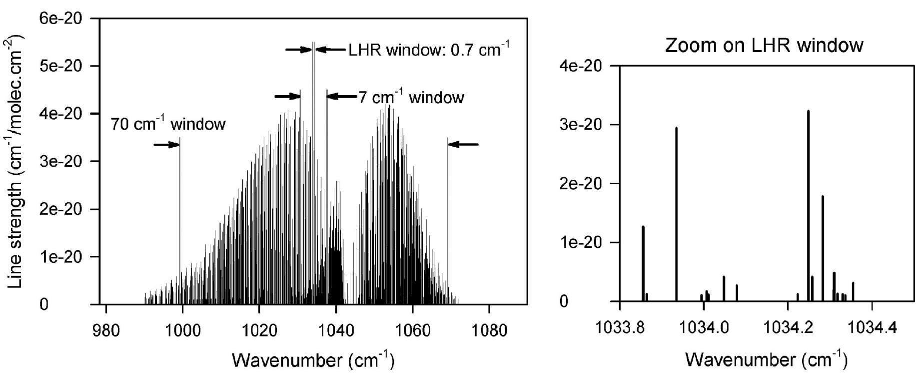

Fig. 3. Plot of the ν_3 band of ozone. The three different spectral windows used to investigate the influence of the frequency coverage on the retrieval quality are indicated. On the right hand side, the LHR window has been expanded.

Table 3. Most Intense Ozone Rovibrational Transitions Occurring within the LHR Window [Line Intensities > 10^{-21} cm^{-1}/(molec. cm^{-2})]

Frequency (cm^{-1})	Intensity @ 296 K (cm^{-1}/(molec. cm^{-2}))	Lower State Energy (cm^{-1})	Band
1033.8556	1.270E-20	108.458	ν_3
1033.8638	1.240E-21	746.628	$\nu_2 + \nu_3 - \nu_2$
1033.9348	2.950E-20	50.302	ν_3
1033.9943	1.120E-21	565.209	ν_3
1034.0057	1.710E-21	547.368	ν_3
1034.0104	1.140E-21	759.942	$\nu_2 + \nu_3$
1034.0472	4.220E-21	504.709	ν_3
1034.0783	2.720E-21	523.866	ν_3
1034.2225	1.270E-21	757.518	$\nu_2 + \nu_3$
1034.2482	3.230E-20	39.75	ν_3
1034.2575	4.220E-21	136.064	ν_3
1034.2821	1.790E-20	80.336	ν_3
1034.3081	1.980E-21	525.527	ν_3
1034.3094	4.890E-21	490.424	ν_3
1034.3180	1.310E-21	540.844	ν_3
1034.3298	1.220E-21	751.459	$\nu_2 + \nu_3 - \nu_2$
1034.3362	1.060E-21	784.868	$\nu_2 + \nu_3 - \nu_2$
1034.3544	3.140E-21	505.384	ν_3

scan across the spectral window. Usually 1% of the central laser frequency can be covered by a change in laser temperature or injection current. Practically, unless one implements a real-time active attenuation system, the laser power varies widely during spectral tuning (from hundreds of microwatts to a few tens of milliwatts). This reduces the useful continuous spectral tuning range. AKs were calculated for three different spectral windows, with a data spacing $\Delta\sigma$:

$$1033.80 \text{ to } 1034.50,\ \Delta\sigma = 0.0007\ cm^{-1},$$

$$1030.65 \text{ to } 1037.65,\ \Delta\sigma = 0.007\ cm^{-1},$$

$$999.15 \text{ to } 1069.15,\ \Delta\sigma = 0.07\ cm^{-1}.$$

These spectral windows are indicated with respect to the ν_3 band of ozone in Fig. 3. Table 3 gives the details of the most intense ozone lines appearing in the LHR window of Fig. 3. The data point spacing of the three windows was set so that the total number of data points remained identical and so did the acquisition time. The results indicate that no improvement arose from using a wider spectral window. In other words, using a carefully selected ozone-specific high-resolution microwindow will provide as much information as a medium-resolution radiometer covering a broad spectral range. This is a key advantage and favors the development of physically small and lightweight LHR instruments over larger and heavier Fourier transform spectroradiometers.

4. Retrieval Results

As mentioned in the section dedicated to the retrieval method, two different sets of *a priori* conditions were tested. The results of the retrievals are shown in

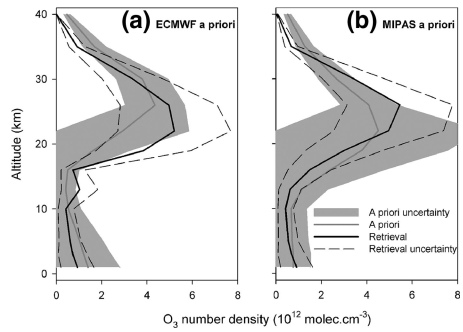

Fig. 4. Ozone vertical profiles retrieved for two different sets of *a priori* conditions.

Fig. 4. Figure 5 shows the corresponding AKs as well as the pressure and temperature profiles used in the forward model. In spite of the two different *a priori* conditions, both retrievals converged toward the same final profile, as indicated in the combined plot of Fig. 6. The retrieved profile based on ECMWF data has a maximum concentration at 22 km (5.2×10^{12} molecules cm^{-3}) compared with 26 km (5.5×10^{12} molecules cm^{-3}) for the retrieval based on the MIPAS standard atmosphere *a priori*. However, the LHR values are in good agreement, and the discrepancy seems to be related to the coarseness of the profile altitude grid, being incapable of resolving the actual peak location. The profile obtained with the ECMWF *a priori* also shows a secondary peak that is not reproduced on the other retrieval.

The AKs appearing in Fig. 5(a) are consistent with the preliminary simulation presented in Section 3. The retrieval was insensitive to atmospheric layers above 40 km. A minimum in sensitivity, and the associated reduction in vertical resolution, can be seen in the range 5 to 15 km, due to the low level of ozone concentration at those altitudes.

The LHR was the only instrument operating during the RAL measurement campaign, and no other local sources of data on ozone profile were available. To provide a comparison with ozone profiles derived from the LHR measurements, data from the Network for the Detection of Atmospheric Composition Change were investigated. Three relevant ozone-

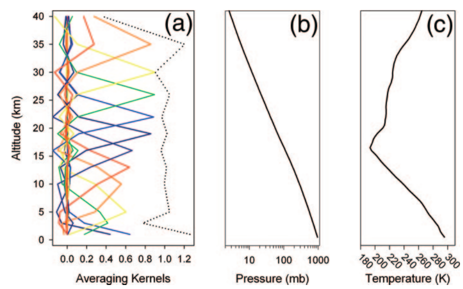

Fig. 5. (Color online) (a) Averaging kernels corresponding to the ECMWF *a priori* retrieval of Fig. 3. (b) Pressure profile and (c) temperature profile interpolated in time and space from the ECMWF dataset.

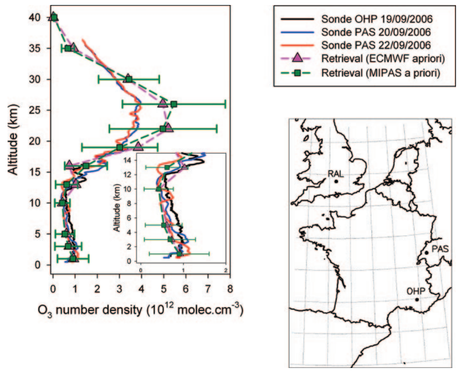

Fig. 6. (Color online) Comparison of the ozone profile retrievals from the LHR measurements at RAL with ozonesonde data from the Observatoire de Haute Provence (OHP) and the Payerne Aerological Station (PAS). The inset within the plot focuses on the tropospheric data. The inset map shows the geographical location of the three sites.

sonde launches were found at northern hemisphere midlatitude locations occurring at around the same time as the LHR measurements. The first launch was on 19 September from the Observatoire de Haute Provence (OHP) located in the French Alps [24], but unfortunately no stratospheric data were recorded during this launch. Two subsequent launches were from the Payerne Aerological Station (PAS), Switzerland, on 20 and 22 September [25]. The locations of the two launch sites and the RAL site are marked on the map shown in Fig. 6. The left hand panel in Fig. 6 shows an excellent agreement between the profiles retrieved from the LHR measurements and the ozonesonde data up to an altitude of 19 km. At higher altitudes the ozonesonde concentrations are approximately 20% lower than those retrieved from the LHR data. A similar effect has been reported by Liu *et al.* concerning profiles retrieved from the satellite-based Global Ozone Monitoring Experiment (GOME) [26]. Liu *et al.* observed large negative biases in stratospheric ozonesonde data, primarily but not exclusively at latitudes lower than 30 °N.

To investigate this discrepancy further the ozone total column data retrieved from the ozone monitoring instrument (OMI) [27] were investigated. Unfortunately no OMI data are available for the exact day of the LHR campaign (21st of September). However, data from the day before and the day after are available. Figure 7 shows contour plots of the ozone total column for these two days. RAL, PAS, and OHP are also indicated on the plot. On the 22nd of September a significant increase (10%) of ozone was observed over RAL (305 DU) compared to PAS (278 DU). If the increase had started on the 21st, this may contribute to the discrepancy at stratospheric altitudes shown in Fig. 6.

At tropospheric levels the relative difference between ozonesonde and LHR data is within $\pm 50\%$. The same relative difference is observed between the data from the two ozonesonde launches from Payerne and is related to the high variability of tropospheric

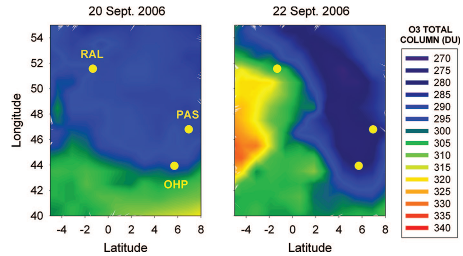

Fig. 7. (Color online) Ozone total column over the Rutherford Appleton Lab (RAL), the Payerne Aerological Station (PAS), and the Observatoire de Haute Provence (OHP) during the two days bracketing the LHR atmospheric campaign. Data are from OMI on the Aura Earth Observing System satellite. On 22nd of September a significant increase in the ozone column above RAL compared to PAS can be seen.

ozone and the fact that measurements are not collocated.

5. Retrieval Analysis

Further information about the sensitivity of the retrieved profile to the measurement vector can be gathered by analyzing the gain matrix $\mathbf{G}$ defined as

$$\mathbf{G} = \left(\mathbf{S_a}^{-1} + \mathbf{K}^T \mathbf{S}_\varepsilon^{-1} \mathbf{K}\right)^{-1} \mathbf{K}^T \mathbf{S}_\varepsilon^{-1}, \tag{5}$$

which gives the contribution of measurement vector channels to the retrieval. The $\mathbf{G}$ matrix allows the mapping of particular spectral features containing information about a specific atmospheric layer. The absolute value of the gain matrix is shown in Fig. 8(c). Also shown are the measurement vector [Fig. 8(d)], the residual after fitting [Fig. 8(e)], and a global gain factor $\mathbf{G}_\Sigma$ [Fig. 8(b)] defined by

$$\mathbf{G}_\Sigma = \sqrt{\sum_{i=1}^{m} (\mathbf{G}_i)^2}, \tag{6}$$

$\mathbf{G}_i$ being the column vectors of the gain matrix as represented in Fig. 8(c). $\mathbf{G}_\Sigma$ gives the altitudinal sensitivity of the retrieval to the measurement vector as a whole. $\mathbf{G}_\Sigma$ exhibits large values in the 10 to 20 km layer. The gain matrix indicates which channels of the measurement vector contribute the most, and consequently which spectral features provide the most relevant ozone information in this atmospheric layer. The quadruplet at 1034.05 cm^{-1} and the first peak at 1033.85 cm^{-1} are the main contributors. Likewise, lower troposphere information comes from the four absorption peaks at 1034.15 cm^{-1}. Once again this demonstrates that a high-resolution instrument that can resolve a few well-defined lines over an extremely narrow spectral range is sufficient to retrieve useful profile information.

The retrieval errors are characterized in our case by the smoothing error covariance matrix $\mathbf{S_S}$ taking into account the finite vertical resolution of the observing system, and the retrieval noise covariance matrix $\mathbf{S_N}$ describing the error purely due to the measurement uncertainty. The main error contribution

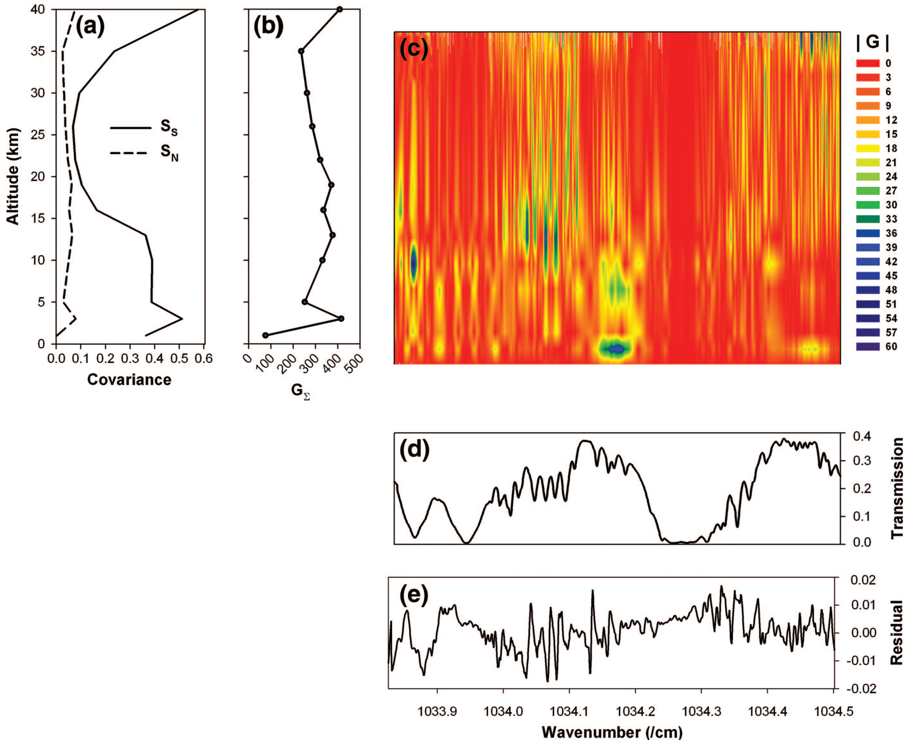

Fig. 8. (Color online) Retrieval error analysis plots: (a) the diagonal elements of the smoothing error and retrieval noise covariance matrices, (b) the global gain factor, (c) the absolute value of the gain matrix, (d) the corresponding measurement vector, and (e) the corresponding residual between the measurement vector and the forward model applied to the retrieved state.

arises from the diagonal elements; Fig. 8(a) shows a plot of these. The smoothing error is the major contribution. High gain values also mean high sensitivity to noise. The correlation between $\mathbf{S_N}$ [Fig. 8(a)] and $\mathbf{G_\Sigma}$ [Fig. 8(b)] is obvious. Ideally the noise present in the channels that contribute the most information should be minimized. Looking at the residual in Fig. 8(e), derivativelike peaks are noticeable in highly contributing channels. These peaks are most probably due to a slight nonlinear frequency miscalibration (assuming that line parameters taken from the HITRAN 2004 database are correct) originating from the frequency calibration of the QCL [1,23]. This problem is currently being solved, and the quality of the retrieval will certainly be improved. Other secondary sources of error include errors in the profile concentration of the interfering species (the most contributing ones being H_2O and CO_2, with an optical depth 1000 smaller than the ozone), the baseline correction [1], local oscillator power modulation, and spurious optical feedback in the quantum cascade laser.

6. Information Analysis

Information analysis is helpful to accurately quantify how our knowledge on the atmospheric state has been improved by the LHR measurements. The full description on the information analysis can be found in Ref. [18]. Briefly, as linear transformations do not alter the information content, the idea consists of performing a basis change to the $\mathbf{K}$ matrix to turn it into a diagonal matrix $\tilde{\mathbf{K}}$ scaled by the roots of the *a priori* and measurement covariances. The forward model from Eq. (4) can be rewritten:

$$\tilde{\mathbf{y}} = \tilde{\mathbf{K}}\tilde{\mathbf{x}} + \tilde{\varepsilon}. \tag{7}$$

The identification of singular values λ_i and corresponding singular vectors (SVs) then allows the identification of the independent sources of information. Following Ref. [18], the total Shannon information content is given by

$$H = \sum_i \frac{1}{2} \log(1 + \lambda_i^2), \tag{8}$$

and the total number of independent quantities measured is given by the degree of freedom for the signal:

$$d = \sum_i \frac{\lambda_i^2}{(1 + \lambda_i^2)}. \tag{9}$$

Applied to the retrieval presented above, the information content is 47.8 bits and the total degree of freedom is 8.5.

Figure 9 shows the first twelve most significant SVs of the $\tilde{\mathbf{K}}$ matrix. The first six exhibit a full degree of freedom. SV1 and SV2 have extrema at ground level and at 22 km, indicating that the true state contributes significantly to the retrieved state at

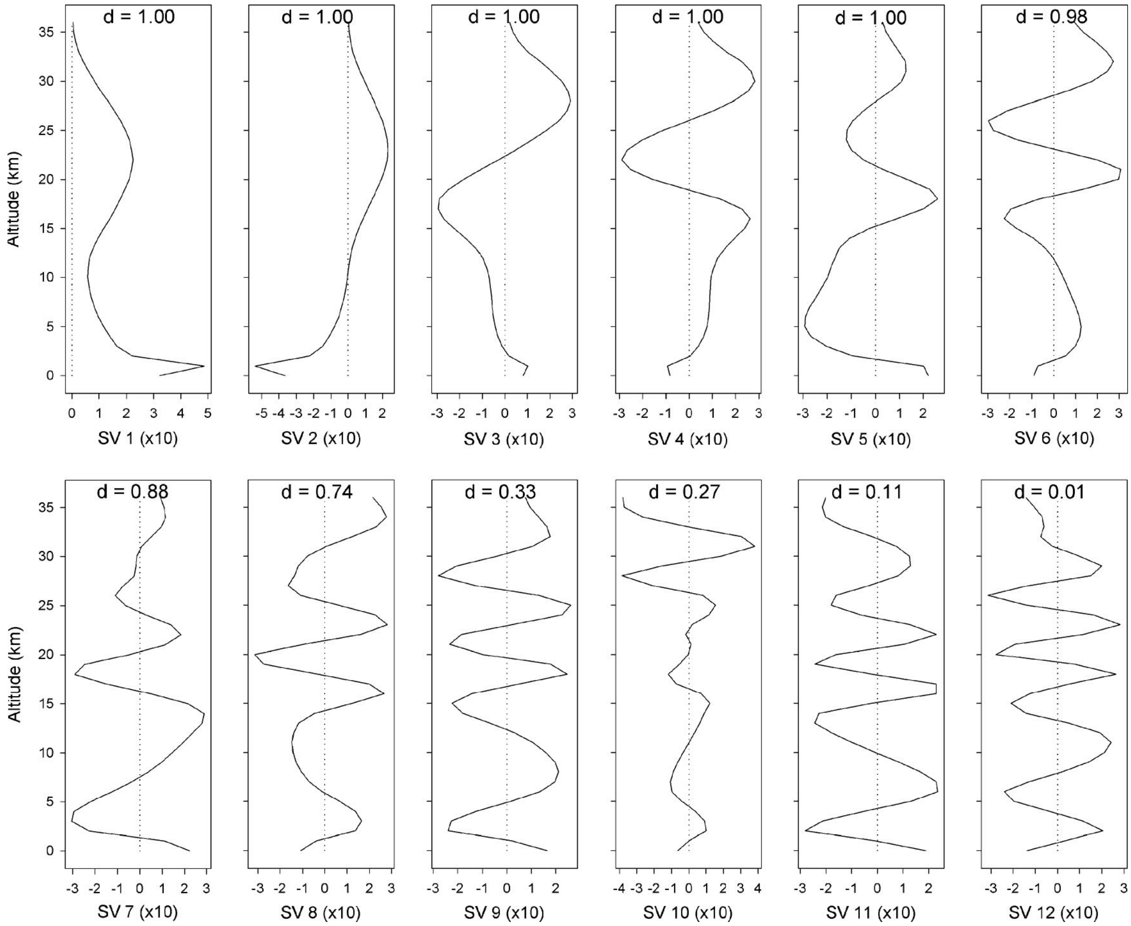

Fig. 9. First twelve and most significant singular vectors (SVs) of the $\tilde{\mathbf{K}}$ matrix. These vectors describe the altitudinal location of each independent piece of information retrieved. The corresponding individual degree of freedom, d, quantifies whether the SVs contribute significantly ($d \approx 1$) to the knowledge of the true atmospheric state, or merely reproduce the *a priori* conditions ($d \ll 1$).

these levels. The next three SVs also show excellent sensitivity to the boundary layer and the stratosphere (up to 32 km). Less information can be recovered from the upper tropospheric layer between 5 and 15 km. The first SV showing sensitivity to this region (number nine) only contributes about one third of a degree of freedom. This lack of sensitivity in the upper troposphere was also perceptible in the AKs. Above the twelfth SV the retrieval does not contribute information about the true atmospheric state ($d < 0.01$) and simply reproduces the *a priori* conditions.

7. Conclusion and Prospects

As part of the characterization and evaluation of a recently developed QCL-based laser heterodyne radiometer for atmospheric sounding, retrieval of atmospheric ozone profiles from ground-based measurements in solar occultation mode have been presented. The retrieval algorithm was based on the optimal estimation method developed by C. Rodgers [18]. The retrievals and subsequent analysis have demonstrated the excellent performance achieved by the prototype LHR instrument: typically 2 and 3 km vertical resolution in the lower troposphere and stratosphere, respectively. Comparisons with ozonesonde data from northern hemisphere midlatitude locations showed good agreement with LHR retrievals, with the notable exception of stratospheric concentrations that appeared to be 20% smaller than those derived from the LHR measurements. Information analysis showed that retrievals from LHR measurements provided a high level of information about the true atmospheric state. Error analysis has provided an insight into the issues that must be addressed to deliver improved performance. In particular, local oscillator frequency calibration issues associated with laser frequency sweeping need to be resolved. The temporal variation of the solar background signal (caused by atmospheric effects, e.g., subvisible clouds) and local oscillator power modulation must also be integrated in the forward model.

The current QCL-based LHR has a dimension of 75 cm × 75 cm. There is huge potential for miniaturization through optical integration. The combination of ultrahigh spectral resolution, high spatial resolution, high sensitivity, and compact physical size that this type of radiometer can offer is ideally suited to future aircraft and space missions. It has also been demonstrated that the narrow spectral microwindow accessible with a QCL local oscillator does not reduce the quality of retrievals, compared to lower resolution broadband radiometers, provided that the local oscillator frequency is carefully chosen according to the target species.

The LHR is part of an ongoing program of instrument development at RAL, and significant improvements are in progress. In particular, measurements of atmospheric emission are planned, together with a comprehensive analysis of predicted performance for a LHR deployed on various types of observation platform (aircraft, high altitude platforms, sun-synchronous, polar-orbiting, and geostationary satellites) for various viewing geometries (nadir, limb, solar, and lunar occultation modes).

D. Weidmann is very grateful to the organizers and participants of the 2005 Oxford/RAL Spring School in Quantitative Earth Observation where many concepts used in this paper were practiced and discussed.

The authors wish to thank Barry Latter from the Space Science and Technology Department of the Rutherford Appleton Laboratory for his computing assistance.

Ozonesonde data used in this publication were obtained as part of the Network for the Detection of Atmospheric Composition Change (NDACC) and is publicly available (see http://www.ndacc.org).

We acknowledge the European Centre for Medium-Range Weather Forecasts and the British Atmospheric Data Centre for the provision of the operational atmospheric profiles.

This research was supported by the Natural Environment Research Council (grant reference NER/Z/S/2003/00642).

References

1. D. Weidmann, W. J. Reburn, and K. Smith, "Ground-based prototype quantum cascade laser heterodyne radiometer for atmospheric studies," Rev. Sci. Instrum. **78,** 073107 (2007).
2. P. L. Kinney, "The pulmonary effects of ozone and particle air pollution," Sem. Respir. Crit. Care Med. **20,** 601–607 (1999).
3. R. T. Menzies and R. K. Seals, "Ozone monitoring with an infrared heterodyne radiometer," Science **197,** 1275–1277 (1977).
4. M. A. Frerking and D. J. Muehler, "Infrared heterodyne spectroscopy of atmospheric ozone," Appl. Opt. **16,** 526–528 (1977).
5. M. M. Abbas, T. Kostiuk, M. J. Mumma, D. Buhl, V. G. Kunde, and L. W. Brown, "Stratospheric ozone measurement with an infrared heterodyne spectrometer," Geophys. Res. Lett. **5,** 317–320 (1978).
6. M. Taguchi, S. Okano, H. Fukunishi, and Y. Sasano, "Comparison of ozone profiles from ground-based laser heterodyne spectrometer and ozonesonde measurements," Geophys. Res. Lett. **17,** 2349–2352 (1990).
7. Y. J. Meijer, D. P. J. Swart, F. Baier, P. K. Bhartia, G. E. Bodeker, S. Casadio, K. Chance, F. Del Frate, T. Erbertseder, M. D. Felder, L. E. Flynn, S. Godin-Beekmann, G. Hansen, O. P. Hasekamp, A. Kaifel, H. M. Kelder, B. J. Kerridge, J.-C. Lambert, J. Landgraf, B. Latter, X. Liu, I. S. McDermid, Y. Pachepsky, V. Rozanov, R. Siddans, S. Tellmann, R. J. van der A, R. F. van Oss, M. Weber, and C. Zehner, "Evaluation of Global Ozone Monitoring Experiment (GOME) ozone profiles from nine different algorithms," J. Geophys. Res. **111,** D21306, doi:10.1029/2005JD006778 (2006).
8. P.-F. Coheur, B. Barret, S. Turquety, D. Hurtmans, J. Hadji-Lazaro, and C. Clerbaux, "Retrieval and characterization of ozone vertical profiles from a thermal infrared nadir sounder," J. Geophys. Res. **110,** D24303, doi:10.1029/2005JD005845 (2005).
9. M. Palm, C. v. Savigny, T. Warneke, V. Velazco, J. Notholt, K. Künzi, J. Burrows, and O. Schrems, "Intercomparison of O_3 profiles observed by SCIAMACHY and ground based microwave instruments," Atmos. Chem. Phys. **5,** 2091–2098 (2005).
10. A. J. Geer, W. A. Lahoz, S. Bekki, N. Bormann, Q. Errera, H. J. Eskes, D. Fonteyn, D. R. Jackson, M. N. Juckes, S. Massart, V.-H. Peuch, S. Rharmili, and A. Segers, "The ASSET intercomparison of ozone analyses: method and first results," Atmos. Chem. Phys. **6,** 5445–5474 (2006).
11. M. De Maziere, O. Hennen, and M. Van Roozendael, "Daily ozone vertical profile model built on geophysical grounds, for column retrieval from atmospheric high resolution infrared spectra," J. Geophys. Res. **104,** D19, 23855–23869 (1999).
12. B. Barret, M. De Maziere, and P. Demoulin, "Retrieval and characterization of ozone profiles from solar infrared spectra at the Jungfraujoch," J. Geophy. Res. **107,** D24, 4788, doi:10.1029/2001JD001298 (2002).
13. C. Brogniez, M. Houët, A. M. Siani, P. Weihs, M. Allaart, J. Lenoble, T. Cabot, A. de la Casinière, and E. Kyrö, "Ozone column retrieval from solar UV measurements at ground level: effects of clouds and results from six European sites," J. Geophys. Res. **110,** **D24202,** doi:10.1029/2005JD005992 (2005).
14. X. Liu, K. Chance, C. E. Sioris, M. J. Newchurch, and T. P. Kurosu, "Tropospheric ozone profiles from a ground-based ultraviolet spectrometer: a new retrieval method," Appl. Opt. **45,** 2352–2359 (2006).
15. P. Keckhut, S. McDermid, D. Swart, T. McGee, S. Godin-Beekmann, A. Adriani, J. Barnes, J.-L. Baray, H. Bencherif, H. Claude, A. G. di Sarra, G. Fiocco, G. Hansen, A. Hauchecorne, T. Leblanc, C. H. Lee, S. Pal, G. Megie, H. Nakane, R. Neuber, W. Steinbrecht, and J. Thayer, "Review of ozone and temperature lidar validations performed within the framework of the Network for the Detection of Stratospheric Change," J. Environ. Monito. **6,** 721–733 (2004).
16. K. E. Fast, T. Kostiuk, F. Espenak, T. A. Livengood, T. Hewagama, and M. F. A'Hearn, "Stratospheric ozone profiles from Mauna Kea, Hawai'i (19.8N, 155.5W) using infrared heterodyne spectroscopy, 1988–2003," Geophys. Res. Lett. **31,** L08109, doi:10.1029/2004GL019443 (2004).
17. K. Fast, T. Kostiuk, F. Espenak, J. Annen, D. Buhl, T. Hewagama, M. F. A'Hearn, D. Zipoy, T. A. Livengood, G. Sonnabend, and F. Smulling, "Ozone abundance on Mars from infrared heterodyne spectra. I. Acquisition, retrieval, and anticorrelation with water vapor," Icarus **181,** 419–431 (2006).
18. C. D. Rodgers, "Inverse Methods for Atmospheric Sounding: Theory and Practice (World Scientific, 2000).
19. I. Petropavlovskikh, P. K. Bhartia, and J. DeLuisi, "New Umkehr ozone profile retrieval algorithm optimized for climatological studies," Geophys. Res. Lett. **32,** L16808, doi:10.1029/2005GL023323 (2005).
20. A. Dudhia, "Reference Forward Model software user's manual," www.atm.ox.ac.uk/RFM/sum.
21. L. S. Rothman, D. Jacquemart, A. Barbe, D. Chris Benner, M. Birk, L. R. Brown, M. R. Carleer, C. Chackerian, K. Chance, L. H. Coudert, V. Dana, V. M. Devi, J.-M Flaud, R. R. Gamache, A. Goldman, J.-M. Hartmann, K. W. Jucks, A. G. Maki, J.-Y. Mandin, S. T. Massie, J. Orphal, A. Perrin, C. P. Rinsland, M. A. H. Smith, J. Tennyson, R. N. Tolchenov, R. A. Toth, J. Vander Auwera, P. Varanasi, and G. Wagner, "The HITRAN 2004 molecular spectroscopic database," J. Quanti. Spectrosc. Radiat. Transfer **96,** 139–204 (2005).

22. "ECMWF data archive services," http://www.ecmwf.int/products/data/archive/.
23. D. Weidmann, K. Smith, and B. Ellison, "Experimental investigation of high-frequency noise and optical feedback effects using a 9.7 mm continuous-wave distributed-feedback quantum cascade laser," Appl. Opt. **46,** 947–953 (2007).
24. M. Beekmann, G. Ancellet, D. Martin, C. Abonnel, G. Duverneuil, F. Eideliman, P. Bessemoulin, N. Fritz, and E. Gizard, "Intercomparison of tropospheric ozone profiles obtained by electrochemical sondes, a ground based lidar and an airborne UV-photometer," Atmos. Environ. **29,** 1027–1042 (1995).
25. J. Staehelin and W. Schmid, "Trend analysis of the tropospheric ozone concentration utilizing the 20-years data set of the ozone balloon soundings over Payerne," Atmos. Environ. **25A,** 1739–1749 (1991).
26. X. Liu, K. Chance, C. E. Sioris, T. P. Kurosu, and M. J. Newchurch, "Intercomparison of GOME, ozonesonde, and SAGE II measurements of ozone: demonstration of the need to homogenize available ozonesonde data sets," J. Geophys. Res. **111,** D14305, doi:10.1029/2005JD006718 (2006).
27. "Total Ozone Mapping Spectrometer," http://jwocky.gsfc.nasa.gov/.